Chemical Physics 90 (1984) 125–136
North-Holland, Amsterdam



# THE $B^2\Sigma$ INTERACTION POTENTIAL FOR Na–Ne DETERMINED FROM $\Pi$–$\Sigma$ INTERFERENCE STRUCTURES IN DIFFERENTIAL SCATTERING CROSS SECTIONS

F. VAN DEN BERG and R. MORGENSTERN

*Fysisch Laboratorium, Rijksuniversiteit Utrecht, Princetonplein 5, 3584 CC Utrecht, The Netherlands*

Received 21 March 1984

We have measured the differential cross sections for scattering of laser-excited $Na(3^2P_{3/2})$ from Ne at thermal collision energies. For the interpretation of the experimental data we performed semi-classical calculations in which spin–rotational effects were taken into account. From the observed $\Pi-\Sigma$ interference structures in the scattering cross sections we extracted detailed information about the $A^2\Pi$ and $B^2\Sigma$ interaction potentials. We found the excited-state potentials to be in excellent agreement with the potentials determined in recent spectroscopic work. The repulsive branch of the $B^2\Sigma$ potential could be accurately determined. An extrapolation with a Lennard-Jones (8,6) potential shape yielded an equilibrium distance $r_m = 15.1 \pm 0.4$ au. By comparing calculated differential cross sections based on model potentials with our experimental data we conclude that the model potentials of Peach are the most reliable theoretical Na*–Ne potentials known today.

## 1. Introduction

For many years experimental and theoretical studies on the alkali–rare-gas interaction have mainly concentrated on the Na–Ar system. These studies have provided accurate knowledge of the ground-state and excited-state potentials for the Na–Ar interaction. Although much effort has been put into the experimental [1–5] and theoretical [6–11] investigation on the Na–Ne system, these studies did not yield concurring descriptions of the interaction potentials for the ground state and first excited state of the Na–Ne system. It was assumed [4] that incorrect interpretations of experimental data were responsible for the different results obtained by the various experimental methods.

From a spectroscopic study on the NaNe van der Waals molecule Ahmad-Bitar et al. [4] obtained a well depth $\epsilon$ and an equilibrium distance $r_m$ of the $A^2\Pi$ potential which were inconsistent with results obtained from line-broadening [2,3] and scattering experiments [1]. For this reason Ahmad-Bitar et al. called in question the semi-classical methods used to generate the potential curves from spectral line data and scattering data. This doubt on semi-classical interpretations could not be removed until more accurate interaction potentials for the excited state of Na–Ne became available.

Interest in the Na–Ne system has been revived by the spectroscopic work of Lapatovich et al. [12] on the NaNe molecule. From an evaluation of the spectroscopic data of Lapatovich et al., Gottscho et al. [13] derived an accurate potential curve for the $A^2\Pi$ excited state and information about the well in the $B^2\Sigma$ potential curve. Through this work it has become possible to compare the results for the interaction potentials obtained by different experimental methods in a more adequate way.

Recently, the discrepancy between the results obtained from spectral line data and high-resolution spectroscopy has been resolved by Havey et al. [14]. They performed new experiments on the far wing of the Na resonance line perturbed by Ne. Using the quasi-static formalism for their analysis of the experimental data they obtained potential curves in agreement with the experimental results of Lapatovich et al. [12] and Ahmad-Bitar et al. [4]. The reliability of the $A^2\Pi$ potential obtained by Havey et al. was confirmed by Pontius

0301-0104/84/$03.00 

and Santo [15] who compared results from the quasi-static formalism with quantum-mechanical calculations.

The discrepancy between the potentials derived from the scattering experiments of Carter et al. [1] and the spectroscopically determined potential of Ahmad-Bitar et al. [4] was explained by Masnou-Seeuws et al. [16]. The latter authors showed that the scattering cross sections measured by Carter et al. were strongly influenced by the interference between $\Pi$ and $\Sigma$ scattering amplitudes. They were able to demonstrate that spin-uncoupling effects caused by the rotation of the internuclear axis are responsible for the occurrence of such $\Pi$–$\Sigma$ interferences and they proposed a semi-classical description which takes the spin–rotational effects into account. Recently, we have shown [17] that this semi-classical description yields calculated cross sections that are practically identical to the cross sections obtained from a quantum-mechanical calculation. In addition, we have demonstrated that the $A^2\Pi$ and $B^2\Sigma$ interaction potentials obtained from spectroscopic work yield differential cross sections that are in reasonable agreement with our experimental data. Therefore, the interpretation of the Na*–Ne scattering data on the basis of the revised semi-classical formalism can now be regarded as a reliable method for obtaining correct interaction potentials.

Our aim in this report is to establish the interaction potentials for the Na*–Ne system from our high-resolution scattering data. Our experimental cross sections are especially sensitive to the repulsive part of the $B^2\Sigma$ potential, which – up to now – has not been probed in other experimental methods. Therefore, we shall concentrate on determining this potential. In calculating the scattering cross sections we shall make use of the accurate $A^2\Pi$ potential reported by Gottscho et al. [13]. In addition, we shall investigate to what extent $A^2\Pi$ potentials obtained by other methods reported in the literature, e.g. model potential calculations, yield theoretical cross sections that are in agreement with our experimental data.

## 2. Experimental arrangement

The experiments reported here were performed in a crossed-beam apparatus described in detail in ref. [18]. In a previous paper [19] we reported the results of the scattering of ground-state Na by Ne and Ar obtained with the same apparatus. A schematic view of the experimental arrangement is shown in fig. 1.

For the measurement of the scattering intensity of excited Na by Ne a laser beam from an argon-ion-laser-pumped ring dye laser was directed perpendicular to the velocity-selected Na beam and the thermal rare-gas beam. The laser light (linearly polarized) was stabilized to the $F = 2 \rightarrow F = 3$ hyperfine transition of the Na $D_2$ line by using an auxiliary Na-beam apparatus. The laser power at the scattering volume was 28 mW (laser spot size $1.4 \times 4.0$ mm$^2$), which was sufficient to saturate the transition.

The experimental method for obtaining differential scattering cross sections for Na*–Ne is given briefly below: For every scattering angle $\theta$ the difference intensity of scattered Na-atoms is measured with the laser beam turned on and off, respectively

$$\Delta I(\theta) = I^{L}(\theta) - I^{0}(\theta). \tag{2.1}$$

If $d\sigma^0/d\Omega$ and $d\sigma^*/d\Omega$ are the differential cross

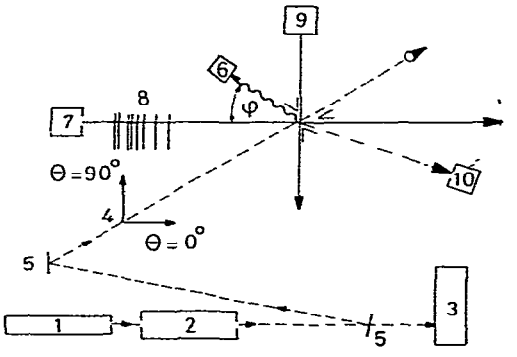


Fig 1. Schematic experimental arrangement (1) $Ar^+$ pump laser, Spectra Physics 164 (2) Spectra Physics 380A cw ring dye laser (3) Auxiliary Na beam apparatus for frequency stabilization. (4) Spectra Physics polarization rotator 310-21 (5) Mirrors (6) Photo-diode as fluorescence monitor (7) Na oven ($T = 470$ K). (8) Mechanical velocity selector. (9) Ne multichannel beam source ($T = 293$ K). (10) Langmuir–Taylor detector + particle multiplier (Bendix M308)

sections for ground-state and excited-state Na scattering, respectively, the difference signal $\Delta I(\theta)$ is proportional to

$$\Delta I(\theta) \propto \alpha d\sigma^*/d\Omega - \alpha d\sigma^0/d\Omega, \qquad (2.2)$$

where $\alpha$ is the fraction of excited Na in the scattering volume. Contributions from background scattering cancel exactly in the difference signal $\Delta I$ since outside the scattering centre the Na projectiles are always in their ground state.

The ground-state and excited-state potentials can be determined by performing fit-calculations of difference scattering patterns and by comparing the calculated results with the experimental difference signals. In principle, we have to take the finite angular resolution of the experiment into account in order to obtain optimum fits of the calculated difference scattering patterns to the experimental data. When the scattering volumes for excited-state and ground-state Na differ, the averaging procedures for the calculated cross sections $d\sigma^0/d\Omega$ and $d\sigma^*/d\Omega$ will be different and become more precarious as the experimental resolution worsens. However, due to the high resolution of our experiment (0.1°) we did not need to average the calculated cross sections over the experimental angular resolution in order to obtain reliable potential curves.

To obtain specific information about the excited-state potentials we selected the range of scattering angles where the ground-state scattering does not produce a structured pattern. The lower limit of this angular range varied from $\approx 8°$ for low collision energies ($E = 2.1 \times 10^{-3}$ au) to $\approx 4°$ for the highest collision energy that we investigated ($E = 4.2 \times 10^{-3}$ au). The upper limit of this range was set by the signal-to-noise ratio of the difference signal and was at most 20°.

In all our scattering measurements we observed a rainbow maximum and rapid oscillations in the angular range selected. The angular positions of the extrema in the rapid oscillations were determined with an accuracy of 0.1°.

The scattering cross sections depend in principle on the applied polarization of the laser light, as was first shown experimentally by Hüwel et al. [20] for Na*–Hg scattering. Recently, Düren et al. [21] have observed coherence effects in K*–Ar scattering experiments using circularly polarized laser light. This indicates the importance of precisely defining the experimental conditions of the excitation process. The quantization axes for excitation ($Z_E$) and scattering ($Z_S$, parallel to the relative velocity vector $g$) must have well-defined relative orientations if the collision process is to be studied in an adequate way. In our experiment we could establish the orientation of $Z_E$ with an accuracy of 2° by measuring the variation in the Na fluorescence ($^2P_{3/2} \rightarrow {}^2S_{1/2}$) intensity while rotating the direction of the linear polarization axis of the laser beam. The fluorescence detector was positioned at a well-established angle $\varphi$ (see fig. 1) in the horizontal plane determined by the Na beam and the laser beam. Before each scattering experiment the direction of the polarization was adjusted parallel to the relative velocity $g$, determined by the Ne velocity ($\bar{v}_{Ne} = 602$ m/s) and the selected Na velocity ($v_{Na} = 800$–$1300$ m/s).

## 3. Survey of the Na*–Ne potentials used

The excited $A^2\Pi$ and $B^2\Sigma$ interaction potentials cannot be determined from the Na*–Ne scattering experiments independently of each other, since the observed oscillation structures in the differential cross sections are due to the interference between the $A^2\Pi$ and $B^2\Sigma$ scattered waves. Therefore, in order to determine the $B^2\Sigma$ potential we shall take advantage of what is known so far about the $A^2\Pi$ interaction for Na–Ne. In table 1 we have listed the equilibrium parameters of the $A^2\Pi$ and $B^2\Sigma$ potentials obtained from theoretical calculations and experiments.

### *3.1. The $A^2\Pi$ potentials*

From a comparison of the experimental $r_m$ values presented it is obvious that the $r_m$ value determined by Carter et al. [1] from an analysis of their scattering data is much larger than the values obtained by other experimental techniques. This discrepancy is due to an incorrect interpretation of the scattering data [16,17].

It is immediately seen from table 1 that the results of the spectroscopic experiments [4,5,12,13]

Table 1
Comparison of equilibrium parameters $\epsilon$ and $r_m$ for the $Na^*$–Ne system obtained from experimental and theoretical methods

| Ref. | $A^2\Pi$ | | $B^2\Sigma$ | | Method [a] | Potential shape |
|---|---|---|---|---|---|---|
| | $\epsilon(10^{-4}$ au) | $r_m$ (au) | $\epsilon(10^{-5}$ au) | $r_m$ (au) | | |
| *Experimental* | | | | | | |
| [1] | 5.5 ±0.7 | 8.0±0.3 | 18.2 | 10.0 | MB | Morse |
| [4] | 6.38±0.15 | 5.1 ±0.1 | 1.1±0.4 | – | SP | RKR |
| [5] [b] | 6.82 | 5.09 | | | | Thakkar |
| [12] | $6.6 \pm^{0.0}_{0.2}$ | 5.1±0.1 | {1.4±0.2} | {14.4±0.3} | SP | LJ(8,6) for $B^2\Sigma$ |
| [13] [c] | 6.58 | 5.16 | 2.0±0.2 | 14.9±0.9 | | Thakkar for $A^2\Pi$ |
| [14] | 7.3 ±0.9 | 5.1±0.1 | | | LS | |
| *Theoretical* | | | | | | |
| [6] | 0.6 | 8.5 | 0.16 | 19.5 | PP | |
| [7] | 0.3 | 9.0 | 0.23 | 20.0 | PP | |
| [10] | 4.0 | 6.0 | | | MP | |
| [8,9] | 6.0 | 5.0 | | | MP | |
| [11] | 6.4 | 5.2 | 2.0 | 14.5 | MP | |
| this work | 6.58 [d] | 5.16 [d] | 2.0 [d] | 15.1±0.4 | MB | LJ(8,6) for $B^2\Sigma$ |

[a] MB: beam scattering experiments; SP: high-resolution laser spectroscopy; LS: line shift and broadening experiment. PP: pseudo-potential calculations; MP: model-potential calculations
[b] Re-evaluation of the experimental data reported in ref. [4] [c] Re-evaluation of the experimental data reported in ref. [12]
[d] These data have been taken from ref. [13], but can be regarded as best-fit results.

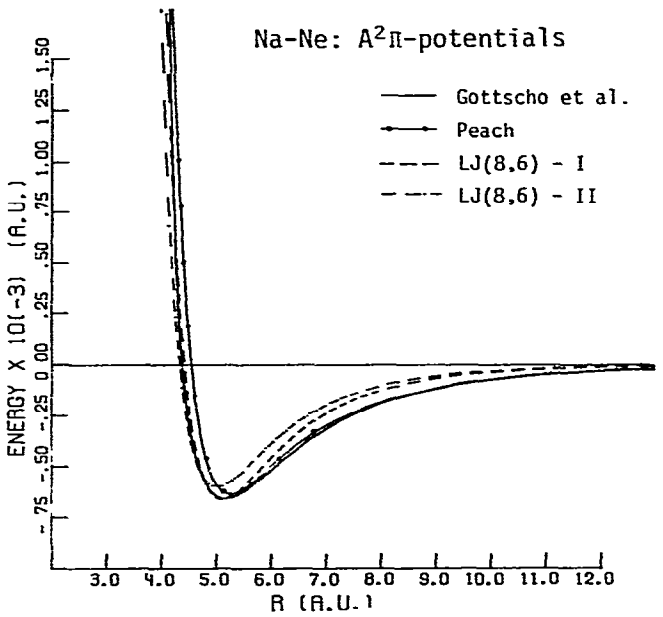


Fig. 2. Interaction potentials for the $A^2\Pi$ state of Na–Ne. The Lennard-Jones (8,6) potential curves I and II were calculated assuming the equilibrium data $\epsilon$, $r_m$ obtained by Lapatovich et al. [12] and Masnou-Seeuws et al. [8], respectively. The $A^2\Pi$ potential of Gottscho et al. [13] was obtained from the Thakkar potential parameters reported by Gottscho et al. The model potential of Peach [11] was provided by Peach as numerical data.

are in excellent mutual agreement and are consistent with the recent line-broadening experiments of Havey et al. [14]. The most detailed description of the $A^2\Pi$ potential curve has been reported by Gottscho et al. [13]. They presented the $A^2\Pi$ potential in an analytical form (Thakkar potential [22]) with parameters fitted to the RKR potential deduced from the spectroscopic data of Lapatovich et al. [12]. This Thakkar potential curve is plotted in fig. 2, together with theoretically calculated potential curves discussed below. In fig. 2 we have also plotted an $A^2\Pi$-potential curve (Lennard-Jones (8,6): LJ(8,6)-I) with the equilibrium data reported by Lapatovich et al. [12].

The slight disagreement between the well depth found by Goble and Winn [5] and Gottscho et al. [13] (see table 1) should not be taken too seriously. Both these equilibrium data were obtained by extrapolating the Thakkar potentials to the dissociation limit. Gottscho et al. noticed that their potential curve was identical within 0.1 $cm^{-1}$ with the curve obtained by Goble and Winn in the region where the RKR potential is valid. However, the Thakkar potential reported by Goble and Winn

does not represent a realistic potential curve at small internuclear distances $r$ because it becomes attractive at $r < 2$ Å.

On the theoretical side the pseudo-potential calculations by Baylis [6] and Pascale and Vandeplanque [7] do not produce acceptable $\epsilon$, $r_m$ values, whereas the model potentials [8–11] are closer to the spectroscopic results. In fig. 2 we show the $A^2\Pi$ potential curve of Peach [11] and an LJ(8,6) potential (LJ(8,6)-II) with equilibrium data $r_m$ and $\epsilon$ as found by Masnou-Seeuws et al. [8]. Fig. 2 illustrates that the model potential of Peach accurately reproduces the attractive part of the Thakkar potential reported by Gottscho et al.

### 3.2. The $B^2\Sigma$ potentials

Much less is known about the $B^2\Sigma$ interaction potential. From an evaluation of the spectra line data of Lapatovich et al. [12], Gottscho et al. [13] obtained accurate values for $r_m$ and $\epsilon$. However, they were not able to generate a reliable RKR potential from the (two) $B^2\Sigma$ vibrational levels given in table 1 by assuming a Lennard-Jones (8,6) shape for the $B^2\Sigma$ potential. The repulsive component of this (8,6) potential deviates from the theoretical model of Peach [11]. Nevertheless the equilibrium data obtained by Peach are in excellent agreement with the depth and position of the potential well determined by Gottscho et al., as can be seen from table 1.

Since the equilibrium parameters of Gottscho et al. [13] are revised $r_m$, $\epsilon$ values of Lapatovich et al. [12] we have bracketed the best-fit values reported by Lapatovich et al. in table 1. The error limits in the $r_m$ value given by Lapatovich et al. seem to be overestimated in view of the larger uncertainty in the $r_m$ result of Gottscho et al.

It should be noted that our scattering experiments probe the repulsive wall, i.e. above the dissociation limit, to which the spectroscopic experiment [12] was not sensitive. So, our experiments can be regarded as being complementary to the spectroscopic investigation on the Na*–Ne molecule [12].

## 4. Results and discussion

### 4.1. Experimental difference scattering patterns

The scattering of laser-excited $Na(3^2P_{3/2})$ by Ne was measured in a range of relative collision energies $E$ from $2.06 \times 10^{-3}$ to $4.22 \times 10^{-3}$ au. Fig. 3 shows the measured scattering cross section at $E = 2.4 \times 10^{-3}$, $3.19 \times 10^{-3}$ and $4.22 \times 10^{-3}$ au. The experimental curve at $E = 3.19 \times 10^{-3}$ au has been presented previously [17] in order to illustrate the accord between semi-classical calculations based on spin-uncoupling effects and the experimental data.

The necessity to take the uncoupling of the spin into account becomes evident from a comparison of the frequency in the experimental rapid oscillations with that predicted theoretically when the spin–orbit ($L$–$S$) coupling is completely neglected (elastic approximation). In this approximation the differential cross section is given by [23,24]

$$\sigma(\theta) = \tfrac{1}{3}|f_\Sigma|^2 + \tfrac{2}{3}|f_\Pi|^2, \tag{4.1}$$

where $f_{\Pi,\Sigma}$ are the amplitudes for elastic scattering in the molecular $A^2\Pi$ and $B^2\Sigma$ state, respectively. In this case the calculated rapid oscillations are due to elastic scattering by the well-known $A^2\Pi$ potential only. The calculated frequency turned out to be significantly lower than the experimental frequency. This can be seen from fig. 4 in which the average experimental as well as the theoretical oscillation periods $\Delta\theta$ are plotted as a function of $1/g$ (with $g$ the relative velocity of the collision partners). Therefore, we have to include in our calculation the uncoupling of the electron spin from the quasi-molecular axis while taking the effective $L$–$S$ coupling at large internuclear distances into account. Then the differential cross section summed over all final states of the scattered Na* atom is given by [16,17]

$$\sigma(\theta) = \tfrac{1}{6}|f_\Pi - f_\Sigma|^2 + \tfrac{1}{3}|f_\Pi|^2 + \tfrac{1}{12}|f_\Pi^- + f_\Sigma^-|^2 + \tfrac{1}{12}|f_\Pi^+ + f_\Sigma^+|^2. \tag{4.2}$$

The amplitudes $f_{\Pi,\Sigma}^{\pm}$ contain phase shifts due to the spin–rotational effects (for further details see ref. [17]). Now the $f_\Pi \cdot f_\Sigma$ terms in (4.2) no longer

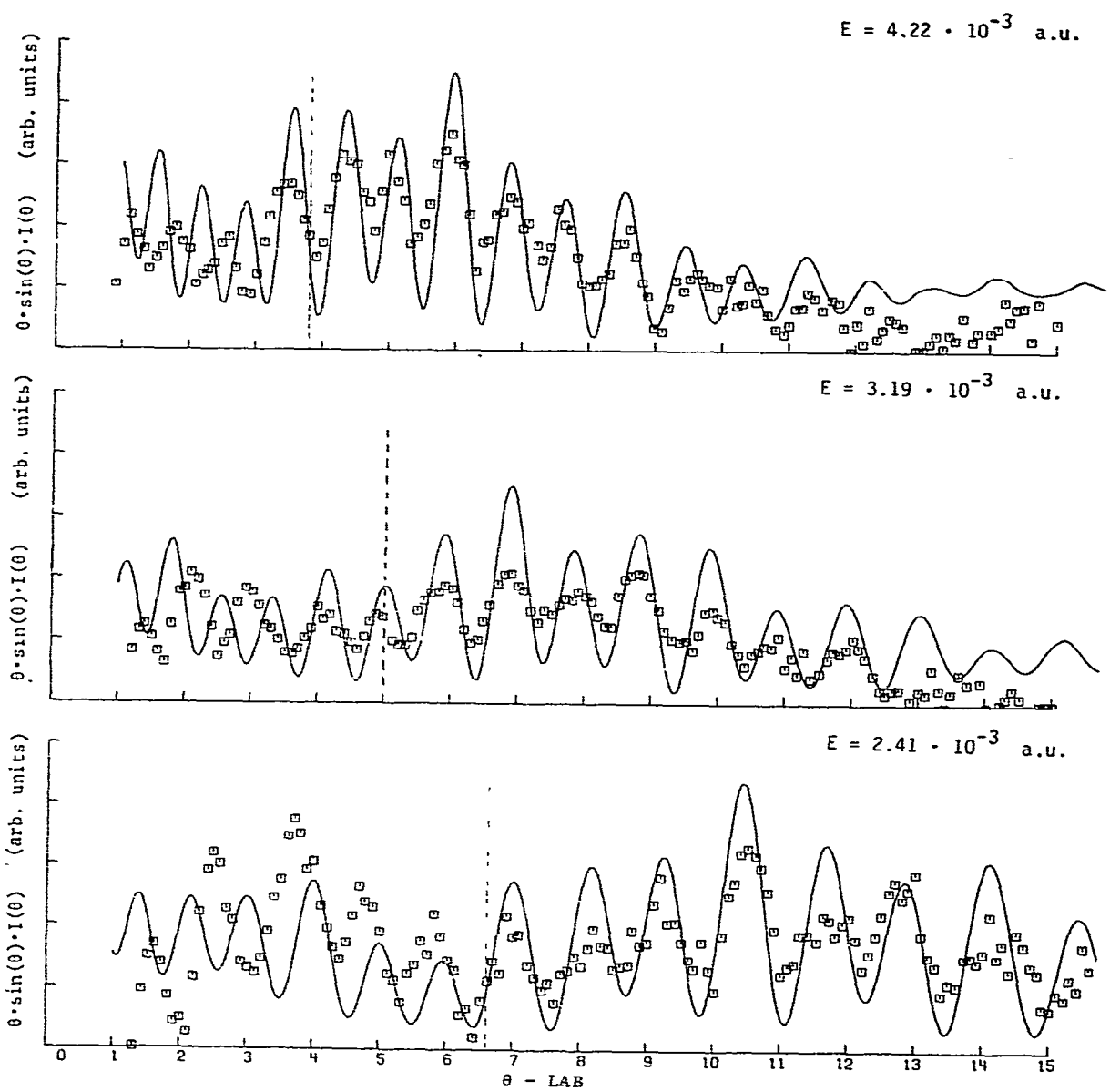


Fig. 3 Differential cross sections for scattering of $Na(3^2P_{3/2})$ by Ne in the lab system □ experimental results (difference between laser on and off signals) ———. results of semi-classical calculations with inclusion of spin-uncoupling effects. The vertical lines indicate the largest scattering angle at which the ground-state scattering influences the oscillation structures in the experimental difference scattering patterns.

cancel each other and consequently the $\Pi$–$\Sigma$ interference strongly influences the scattering pattern. This interference is responsible for the higher experimental oscillation frequency in the observed rapid oscillations, as shown in fig. 4.

In (4.2) it was assumed that the laser light used for the excitation is unpolarized. In the appendix we give the results for the theoretical cross sections obtained with linearly polarized laser light with the polarization vector $\boldsymbol{E}$ parallel as well as perpendicular to the relative velocity $\boldsymbol{g}$ before the collision. In principle the polarization of the alkali

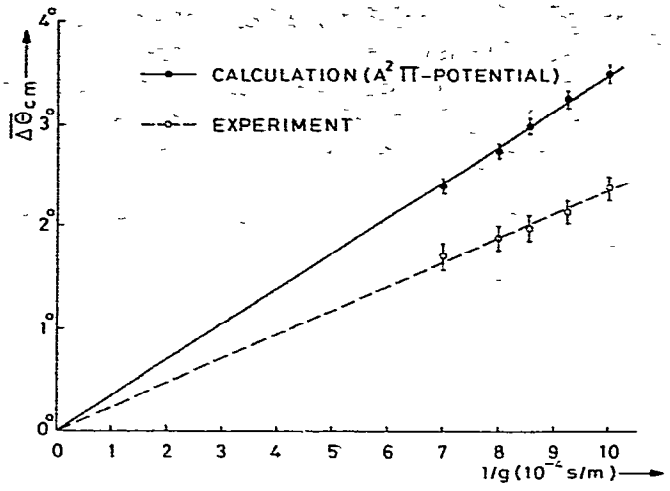


Fig 4 Average angular spacings $\overline{\Delta\theta}$ of the peak positions in the rapid oscillations as a function of $1/g$ The experimental results were transformed to the c m system (open circles). The solid circles represent the results obtained from calculations of differential cross sections of elastic $A^2\Pi$ potential scattering

($^2P_{3/2}$) atom before the collision can influence the scattering pattern as was observed by Hùwel et al. [20] and Dùren et al. [21]. However, our scattering patterns with $E \| g$ did not differ significantly from those with $E \perp g$. This outcome is to be predicted theoretically. In fig. 5 the theoretical scattering patterns for the two cases $E \| g$ and $E \perp g$ are compared with each other and with the case of unpolarized laser light. Obviously, the peak positions in the rapid oscillations are not affected by the laser polarization. Moreover, the relative peak heights in the three unaveraged scattering patterns in fig. 5 would become practically identical if the experimental angular resolution were taken into account in the calculations.

All relevant information about the collision process can be extracted from the angular frequency and the absolute positions of the peaks in the measured oscillatory structure. Consequently, it was sufficient to compare only unaveraged scattering patterns with the experimental patterns. We found that the calculated "best-fit" patterns reproduced the experimental resolution reasonably well. The calculated scattering patterns were considered to be "best-fit" results if the calculated peak positions differed from the experimental positions by less than 0.2° over the whole angular range investigated.

### 4.2. Determination of the $B^2\Sigma$ interaction potential

In order to reproduce the measured cross sections theoretically we started our fitting procedure by taking the interaction potential of Gottscho et al., shown in fig. 1, for the $A^2\Pi$ state and varying the shape and the equilibrium parameters for the $B^2\Sigma$ potential. It should be realized that it is mainly the repulsive part of the $B^2\Sigma$ potential which influences the cross sections in the investi-

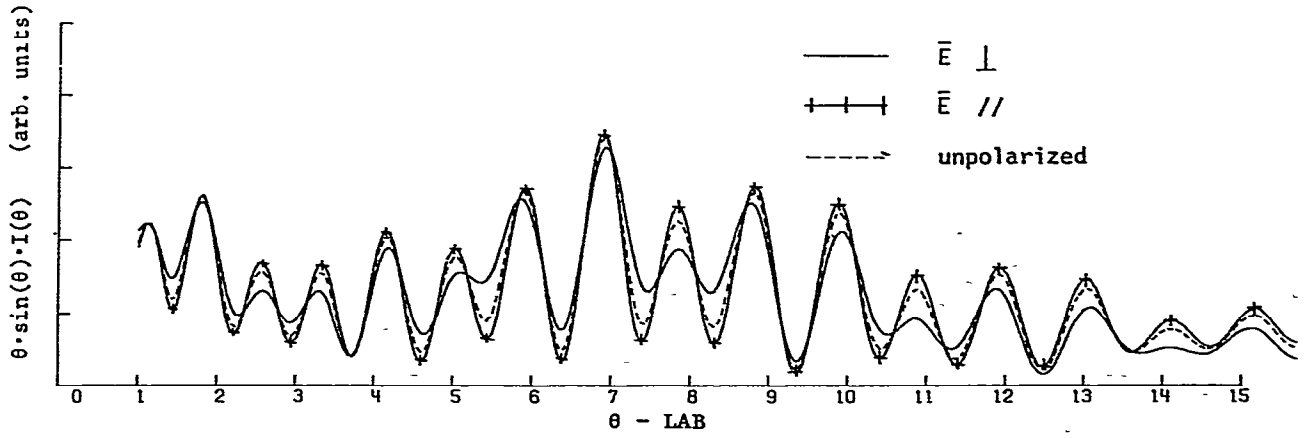


Fig. 5. Calculated differential scattering patterns for the polarization vector $E$ of the laser light parallel and perpendicular to the relative velocity $g$. The collision energy is $3.19\times10^{-3}$ au.

gated angular range. The well depth ($2.06 \times 10^{-5}$ au) is too small to be probed in our experiments. For a fixed shape and well depth of the $B^2\Sigma$ potential the equilibrium distance $r_m$ can be determined from a best fit of the calculated peak positions to the experimental ones. However, one has to bear in mind that the $r_m$ value obtained in this way depends on the chosen potential shape and – to a negligible extent – on the well depth $\epsilon$. The latter was taken equal to the value obtained by Gottscho et al. (see table 1). For a Lennard-Jones ($n$,6) potential with $n = 8$ (as was used by Gottscho et al.) we obtained a best-fit value of $15.1 \pm 0.4$ au for $r_m$. The scattering patterns calculated with these potential parameters are also shown in fig. 3.

There is a high sensitivity of the scattering cross sections on the $r$ position of the repulsive branch of the $B^2\Sigma$ potential. Since our scattering data are not sensitive to the well depth $\epsilon$ we can obtain a relatively small error in $r_m$, provided the assumption of an LJ(8,6) potential shape is correct. The upper and lower limits for $r_m$ given by Gottscho et al. [13], who also assumed the LJ(8,6) shape, can be excluded, as is demonstrated in fig. 6: scattering patterns calculated with these $r_m$ values oscillate largely out of phase with respect to the corresponding measured pattern. On the other hand, their data allow an $\epsilon$ determination which is not possible from our scattering data.

If other ($n$,6) potential shapes are used in the calculations, we obtain different best-fit values for $r_m$. These are plotted in fig. 7a as a function of $n$. In fig. 7b we show the LJ($n$,6) potential curves for $n = 8$, 12, 14 obtained with the corresponding $r_m$ values. These curves are very similar in spite of their different potential parameters $n$ and $r_m$. Since the $r_m$ value of the LJ(8,6) potential is in excellent agreement with the spectroscopically determined value it can be concluded that our LJ(8,6) potential is consistent with the LJ(8,6) potential obtained by Gottscho et al. Furthermore, fig. 7 indicates that the LJ(8,6) shape is the most realistic one. The other shapes investigated yield $r_m$ values that are in less agreement with the $r_m$ value reported by Gottscho et al. In fig. 7 it is assumed that the $r_m$ value obtained by Gottscho et al. does not depend on the repulsive part of the $B^2\Sigma$ potential, determined by the value of $n$. This assumption is justified on the following grounds: (i) in the spectra line measurements of Lapatovich et al. two vibrational levels with their corresponding rotational levels were resolved, which fix the bound part of the potential at the two vibrational levels within the stated error limits; (ii) the error limits of the $r_m$, $\epsilon$ values in the (8,6) potential of Gottscho et al. reflect the uncertainties in the experimental data mentioned in (i); (iii) for LJ($n$,6) potential curves with $n = 12$, 14 the widths of the potential wells are significantly smaller than the width of the LJ(8,6) potential.

We further explored the sensitivity of the cross

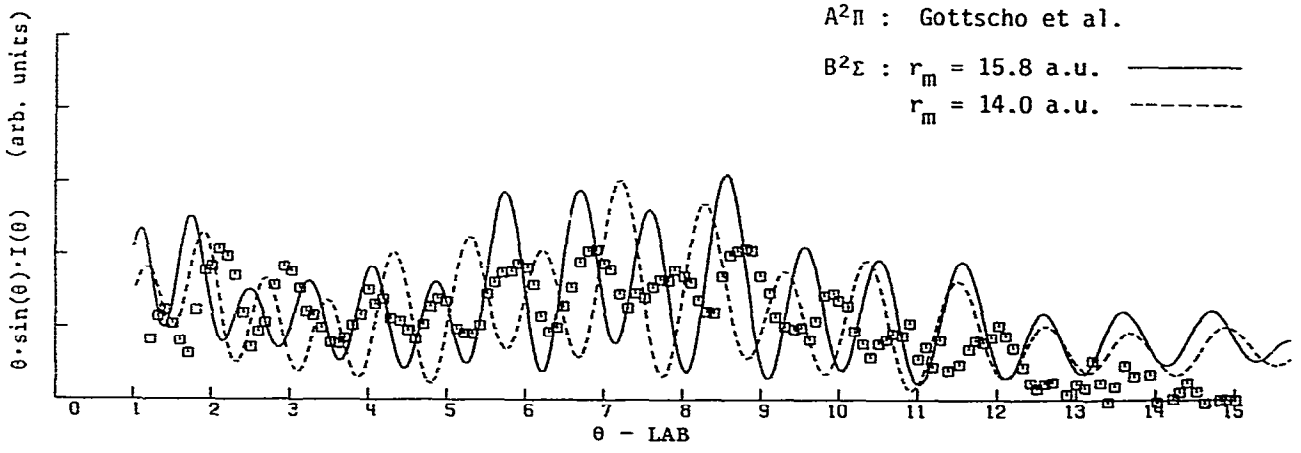


Fig. 6. Comparison of calculated scattering patterns with the experimental result at $E = 3.19 \times 10^{-3}$ au. The $r_m$ values for the $B^2\Sigma$ potential used are the upper and lower $r_m$ limit of the potential reported by Gottscho et al. [13]. The well of the $B^2\Sigma$ potential was taken equal to the $\epsilon$ value obtained by Gottscho et al.

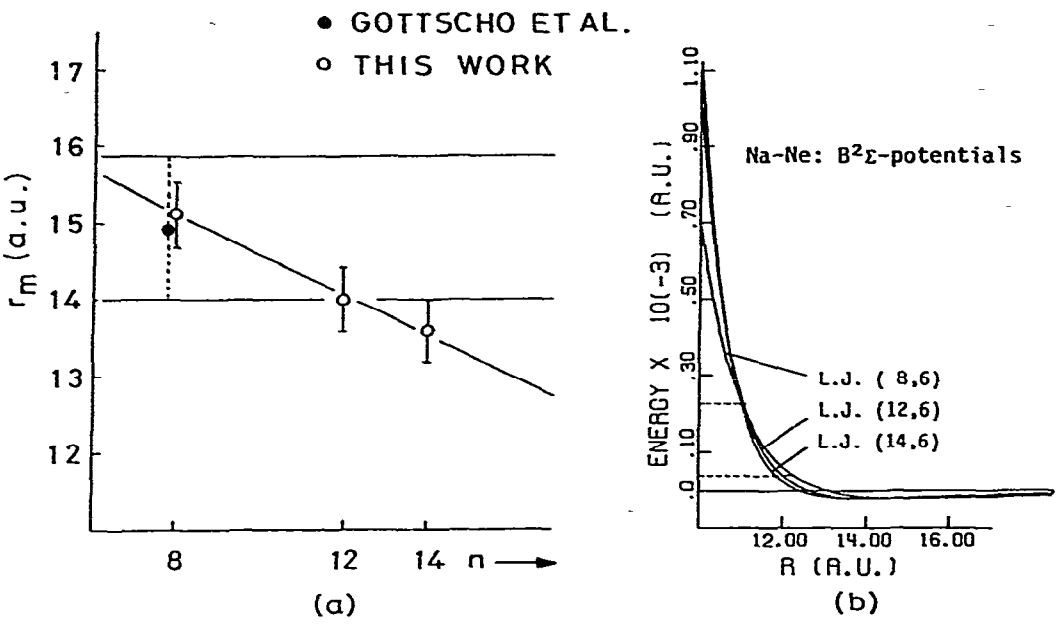


Fig. 7. (a) The best-fit values for $r_m$ of the $B^2\Sigma$ potential obtained with different LJ($n$,6) shapes (open circles). The $r_m$ value obtained by Gottscho et al. [13] is assumed to be independent of the parameter $n$. The horizontal lines present the error limits of the $r_m$ values reported by Gottscho et al. (b) LJ($n$,6) potential curves with $r_m$ values depicted in fig. 7a. In all LJ potential curves the well depth is equal to $2.05 \times 10^{-5}$ au. Our experiments are sensitive to the part of the (8,6) potential indicated by the horizontal dashed lines.

sections to the shape of the $B^2\Sigma$ potential by calculating difference scattering patterns based on the $A^2\Pi$ potential of Gottscho et al. and the theoretical $B^2\Sigma$ model potential calculated by Peach [11]. The well in the $B^2\Sigma$ potential curve of Peach [11] is similar to the well obtained by Gottscho et al. (see table 1). From a comparison of both potential curves it was observed that the repulsive branch of the Peach potential is less steep than the LJ (8,6) potential of Gottscho et al. We found that the scattering patterns calculated with the $B^2\Sigma$ potential of Peach did not fit our experimental scattering data as favourable as those calculated with our best-fit $B^2\Sigma$ potentials. The positions of the peaks could not be reproduced in the entire relevant angular range investigated by us. The experimental oscillation frequency was only reproduced at the intermediate scattering angles, but definitely not at scattering angles larger than the rainbow angle of the $A^2\Pi$ potential. This is a direct consequence of the soft slope of the $B^2\Sigma$ potential of Peach.

### 4.3. Sensitivity to the $A^2\Pi$ potential

Of course, our results for the $B^2\Sigma$ potential depend on the assumed $A^2\Pi$ potential. In our previous investigation [17] we used the LJ(8,6) potential of Lapatovich et al. (shown in fig. 2) for the interpretation of our scattering data. Obviously, the shape of this potential does not reproduce the potential curve deduced by Gottscho et al. If we assume this LJ(8,6) potential (LJ(8,6)-II in fig. 2) for the $A^2\Pi$ state, we have to shift the $r_m$ of the $B^2\Sigma$ potential (LJ($n$,6) with $n = 8$) to higher $r$ values by 1.0 au in order to obtain agreement between the calculated and experimental scattering patterns. Since this $r_m$ value is inconsistent with the value obtained by Gottscho et al. it is concluded that the LJ(8,6)-II potential in fig. 2 is not correct.

We have also applied the theoretical $A^2\Pi$ potential of Peach [11] in the calculations. The peak positions in the calculated scattering patterns could be fitted to the experimentally obtained

positions by taking the $r_m$ value of the $B^2\Sigma$ potential equal to 15.1 au. In fact, the calculated scattering patterns turned out to differ from the patterns calculated with the $A^2\Pi$ potential of Gottscho et al. mainly in peak positions at large scattering angles ($\theta > 15°$). This result is not surprising. The $A^2\Pi$ potentials of Peach and Gottscho et al. differ only in the repulsive part. The contribution of the centrifugal term in the effective $A^2\Pi$ potential decreases the influence of the differences between the potentials of Peach and Gottscho et al. at large impact parameters. However, at small impact parameters (or large scattering angles) this difference between the potential curves is still noticeable in the scattering cross sections. Nevertheless, the relative peak heights in the result obtained with the Peach potential are in less agreement with the experimental result than the experimental and theoretical curves shown in fig. 3. Thus, we can conclude that for the description of the scattering process the $A^2\Pi$ potential obtained by Gottscho et al. is the most realistic one among the various potential curves that we have investigated.

Finally, we note that the well in the theoretical $A^2\Pi$ potential of Masnou-Seeuws et al. [8] is too shallow to produce a reasonable fit of calculated scattering patterns to our experimental results. In their analysis of the scattering data of Carter et al. [1], Masnou-Seeuws et al. [16] already pointed out that the value of $\epsilon$ in their model potential had to be increased in order to reproduce the position of the experimental rainbow maximum measured by Carter et al. This conclusion is consistent with our observations.

## 5. Summary and conclusions

We have been able to establish the $B^2\Sigma$ interaction potential for the Na*–Ne system from an evaluation of our differential scattering experiments and to test the $A^2\Pi$ potentials reported in the literature. We extracted information about these potentials from the rapidly oscillating $\Pi$–$\Sigma$ interference structure observed in the experimental scattering patterns. In order to interpret this interference structure quantitatively it was essential to include spin–rotational effects in the theoretical treatment of the scattering process.

Our result for the $B^2\Sigma$ potential is in excellent agreement with the experimental potential obtained from spectroscopic studies [12,13] provided we use an LJ(8,6) shape in calculating the scattering patterns. This shape was also assumed by Gottscho et al. [13]. Our scattering experiments have allowed us to derive the equilibrium parameter $r_m$ of the $B^2\Sigma$ potential with an accuracy that exceeds that of the most accurate value reported up to now. The $r_m$ value in the $B^2\Sigma$ potential was obtained by extrapolating the accurately determined repulsive part of the LJ(8,6) potential to the well. In addition, we have shown that other potential shapes (LJ($n$,6)) yield "best-fit" $r_m$ values that are inconsistent with the spectroscopically determined $r_m$ values for the $B^2\Sigma$ potential.

On the basis of a comparison of calculated and experimental scattering patterns we conclude that the $A^2\Pi$ potential derived by Gottscho et al. [13] describes the $A^2\Pi$ state interaction in the scattering process more accurately than the other $A^2\Pi$ potentials we investigated.

The shape of the $A^2\Pi$ potential proposed by Gottscho et al. deviates from an LJ(8,6) shape in the attractive part. We have observed that when this (8,6) shape is used in the calculations the "best-fit" $B^2\Sigma$ potential is inconsistent with the result obtained by Gottscho et al. Therefore, accurate knowledge of the shape of the $A^2\Pi$ potential curves is required in order to obtain reliable $B^2\Sigma$ potential curves from the scattering data.

With regard to the theoretical potentials, the model potential calculations seem to reach a level of accuracy that can compete with experimentally obtained potentials. From our best-fit calculations we conclude that the most reliable $A^2\Pi$ and $B^2\Sigma$ model potential curves have been obtained by Peach [11]. The repulsive branches of the $A^2\Pi$ and $B^2\Sigma$ potentials of Peach are, however, too steep and too soft, respectively, to reproduce our experimental scattering patterns.

## Acknowledgement

We thank Professor C.Th.J. Alkemade for his continuous interest in this work, his careful read-

ing of the manuscript and many suggestions for improvements. This work was performed as part of the research programme of the "Stichting voor Fundamenteel Onderzoek der Materie (FOM)", which is financially supported by the "Nederlandse Organisatie voor Zuiver-Wetenschappelijk Onderzoek (ZWO)".

## Appendix. Calculation of scattering cross sections

### *A.1. The density matrices*

With linearly polarized light the initial state of the Na atom is described in a system where the $z$ axis, $Z_E$, is parallel to the electric vector $E$ of the incident light. The optical pumping process populates the hyperfine states $|F_u M_u\rangle$ with $F_u = 3$ from the ground states $|F_l M_l\rangle$ with $F_l = 2$. Under stationary conditions the preparation of the excited states is described by the density operator that satisfies the relation [25]

$$\rho_{M_u M_u'} = \delta_{M_u M_u'}[2(F_l + F_u) + 1] \times \begin{Bmatrix} F_l & F_u & F_l + F_u \\ M_l & -M_u & 0 \end{Bmatrix}^2. \tag{A1}$$

In the case of degenerate hyperfine- and fine-structure states the density matrix for the $|LM_L\rangle$ state is readily obtained from (A1) by taking the trace over nuclear and electronic spin [26]

$$\rho^{(1)} = \frac{1}{9}\begin{pmatrix} 2 & 0 & 0 \\ 0 & 5 & 0 \\ 0 & 0 & 2 \end{pmatrix}. \tag{A2}$$

In a coordinate system with the $z$ axis perpendicular to $Z_E$ the density matrix as given by (A3) is transformed to this new system of reference by

$$\rho^{(2)}_{M'M} = \sum_{m'm} D^1_{M'm'}(0, -\tfrac{1}{2}\pi, 0)\rho^{(1)}_{m'm} D^1_{mM}(0, \tfrac{1}{2}\pi, 0), \tag{A3}$$

where $D^1_{M'M}(\alpha, \beta, \gamma)$ are the rotation matrix elements, e.g. given in ref. [27]. From (A3) one obtains

$$\rho^{(2)} = \frac{1}{18}\begin{pmatrix} 7 & 0 & -3 \\ 0 & 4 & 0 \\ -3 & 0 & 7 \end{pmatrix}. \tag{A4}$$

### *A.2. The scattering intensities*

The intensity $I$ of scattered $Na(3\,^2P_{3/2})$ atoms is given by

$$I = \mathrm{Tr}(\mathbf{F}\cdot\rho\cdot\mathbf{F}^\dagger). \tag{A5}$$

The scattering amplitude matrix $\mathbf{F}$ is described in a system of reference with the $z$ axis perpendicular to the scattering plane. The matrix elements of $\mathbf{F}$ are given by [17]

$$\begin{aligned} F_{11} &= \tfrac{1}{2}(f^-_\Pi + f^-_\Sigma), \\ F_{13} &= \tfrac{1}{2}(f_\Pi - f_\Sigma)^* \exp[-\mathrm{i}(\pi - \theta)], \\ F_{31} &= \tfrac{1}{2}(f_\Pi - f_\Sigma)^* \exp[\mathrm{i}(\pi - \theta)], \\ F_{33} &= \tfrac{1}{2}(f^+_\Pi + f^+_\Sigma), \\ F_{12} &= F_{21} = F_{23} = F_{32} = 0, \end{aligned} \tag{A6}$$

with $f_{\Pi,\Sigma}$ the elastic scattering amplitudes for $A\,^2\Pi$ and $B\,^2\Sigma$ scattering, $f^{\pm}_{\Pi,\Sigma}$ the scattering amplitudes with phase shifts $2\eta'_{\Pi,\Sigma}$ replaced by $2\eta'_{\Pi,\Sigma} \pm 2\phi'_{\Pi,\Sigma}$, where $2\phi'_{\Pi,\Sigma}$ is the rotation of the molecular axis for $A\,^2\Pi$ and $B\,^2\Sigma$ states, respectively. Combining (A2), (A5) and (A6) yields the scattering intensity for $E$ perpendicular to the relative velocity vector $g$:

$$I^\perp = \tfrac{1}{9}|f_\Pi - f_\Sigma|^2 + \tfrac{5}{9}|f_\Pi|^2 + \tfrac{1}{18}|f^-_\Pi + f^-_\Sigma|^2 + \tfrac{1}{18}|f^+_\Pi + f^+_\Sigma|^2. \tag{A7}$$

For $E$ parallel to $g$ the scattering intensity calculated from (A4), (A5) and (A6) is

$$\begin{aligned} I^\parallel = {} & \tfrac{7}{36}|f_\Pi - f_\Sigma|^2 + \tfrac{2}{9}|f_\Pi|^2 \\ & + \tfrac{7}{72}|f^-_\Pi + f^-_\Sigma|^2 + \tfrac{7}{72}|f^-_\Pi + f^-_\Sigma|^2 \\ & - \tfrac{1}{12}\mathrm{Re}(f^+_\Pi + f^+_\Sigma)^*(f_\Pi - f_\Sigma) \\ & \times \exp[\mathrm{i}(\pi - \theta)] \\ & - \tfrac{1}{12}\mathrm{Re}(f^-_\Pi + f^-_\Sigma)^*(f_\Pi - f_\Sigma) \\ & \times \exp[-\mathrm{i}(\pi - \theta)]. \end{aligned} \tag{A8}$$

## References

[1] G. Carter, D. Pritchard, M. Kaplan and T. Ducas, Phys Rev. Letters 35 (1975) 1144.

[2] G. York, R. Scheps and A. Gallagher, J. Chem Phys. 63 (1977) 1052.
[3] N. Lwin, D G McCarten and G L. Lewis, J Phys B9 (1976) L161.
[4] R. Ahmad-Bitar, W P Lapatovich, D E. Pritchard and I Renhorn, Phys Rev Letters 39 (1977) 1657
[5] J H. Goble and J S Winn, J. Chem Phys 70 (1979) 2051.
[6] J E. Baylis, J Chem. Phys. 51 (1969) 2665
[7] J. Pascale and J Vandeplanque, J. Chem. Phys. 60 (1974) 2278
[8] F Masnou-Seeuws, M. Philippe and P. Valiron, Phys Rev Letters 41 (1978) 395.
[9] M Philippe, F. Masnou-Seeuws and P. Valiron, J Phys. B12 (1979) 2493.
[10] A R Malvern and G. Peach, Proceedings of the 10th International Conference on the Physics of Electronic and Atomic Collisions, Paris (1976) p. 230
[11] G Peach, Commun. At. Mol Phys 11 (1982) 101
[12] W P Lapatovich, R. Ahmad-Bitar, P E. Moskowitz, I Renhorn R A. Gottscho and D E. Pritchard, J. Chem Phys 73 (1980) 5419
[13] R A Gottscho, R. Ahmad-Bitar, W.P Lapatovich, I Renhorn and D E. Pritchard, J. Chem. Phys 75 (1981) 3105
[14] M D Havey, S E. Frolking, J J Wright and L C Balling, Phys Rev. A24 (1981) 3105
[15] E.M. Pontius and K.M. Sando, Phys. Rev A28 (1983) 3117.
[16] F. Masnou-Seeuws, M. Philippe, E. Roueff and A. Spielfiedel, J Phys. B12 (1979) 4065
[17] F. van den Berg, P. Bijl and R Morgenstern, Z Physik, submitted for publication
[18] J.M.M van Deventer and F. van der Valk, Physica 112C (1982) 119.
[19] F van den Berg, R. Morgenstern, F van der Valk and C Th J. Alkemade, Z. Physik 312 (1983) 271.
[20] L. Hüwel, J. Maier and H Pauly, J. Chem. Phys. 76 (1982) 4961.
[21] R Düren, E. Hasselbrink and H Tischer, Phys Rev Letters 50 (1983) 1983
[22] A J. Thakkar, J. Chem Phys 62 (1975) 1693
[23] S. Wofsy, R.H G Reid and A Dalgarno, Astrosphys J 168 (1971) 161
[24] R.H G. Reid, J. Phys B8 (1975) L512
[25] I V Hertel and W. Stoll Advan. At Mol Phys 13 (1979) 113.
[26] K. Blum, Density matrix theory and applications (Plenum Press, New York, 1981)
[27] A R Edmonds, Angular momentum in quantum mechanics (Princeton Univ Press, Princeton, 1960)